coatings

Article

Silver Containing Antimicrobial Coatings on Innovative Ti-30Nb-5Mo β-Alloy Prepared by Micro-Arc Oxidation for Biomedical Implant Applications

Giovana Collombaro Cardoso [1,2,*], Katia Barbaro [3], Pedro Akira Bazaglia Kuroda [1], Angela De Bonis [4], Roberto Teghil [4], Valentina Monteleone [3], Luca Imperatori [2], Marco Ortenzi [2], Iulian Antoniac [5,6], Carlos Roberto Grandini [1] and Julietta V. Rau [2,7]

1 Laboratório de Anelasticidade e Biomateriais, UNESP—Universidade Estadual Paulista, Bauru 17033-360, SP, Brazil; pedro.kuroda@unesp.br (P.A.B.K.); carlos.r.grandini@unesp.br (C.R.G.)
2 Istituto di Struttura della Materia, Consiglio Nazionale delle Ricerche (ISM-CNR), Via del Fosso del Cavaliere 100, 00133 Rome, Italy; luca.imperatori@cnr.it (L.I.); marco.ortenzi@ism.cnr.it (M.O.); giulietta.rau@ism.cnr.it (J.V.R.)
3 Istituto Zooprofilattico Sperimentale Lazio e Toscana "M. Aleandri", Via Appia Nuova 1411, 00178 Rome, Italy; katia.barbaro@izslt.it (K.B.); valentina.monteleone-esterno@izslt.it (V.M.)
4 Dipartimento di Scienze, Università della Basilicata, Via dell'Ateneo Lucano 10, 85100 Potenza, Italy; angela.debonis@unibas.it (A.D.B.); roberto.teghil@unibas.it (R.T.)
5 Faculty of Material Science and Engineering, Politehnica University of Bucharest, 313 Splaiul Independentei Street, District 6, 060042 Bucharest, Romania; antoniac.iulian@gmail.com
6 Academy of Romanian Scientists, 54 Splaiul Independentei Street, District 5, 050094 Bucharest, Romania
7 Department of Analytical, Physical and Colloid Chemistry, Institute of Pharmacy, I.M. Sechenov First Moscow State Medical University, Trubetskaya 8, Build. 2, Moscow 119048, Russia
* Correspondence: giovana.collombaro@gmail.com

check for updates

Citation: Cardoso, G.C.; Barbaro, K.; Kuroda, P.A.B.; De Bonis, A.; Teghil, R.; Monteleone, V.; Imperatori, L.; Ortenzi, M.; Antoniac, I.; Grandini, C.R.; et al. Silver Containing Antimicrobial Coatings on Innovative Ti-30Nb-5Mo β-Alloy Prepared by Micro-Arc Oxidation for Biomedical Implant Applications. *Coatings* **2024**, *14*, 214. https://doi.org/10.3390/coatings14020214

Academic Editor: Yanxin Qiao

Received: 12 January 2024
Revised: 1 February 2024
Accepted: 5 February 2024
Published: 7 February 2024

Abstract: Micro-arc oxidation (MAO) is a versatile surface-modification method that promotes higher wear and corrosion resistance, osseointegration, and biological activity to titanium alloys' surfaces. This study aimed to modify the surface of a recently developed metastable β Ti alloy, which exhibits more favorable mechanical properties for implant applications compared to some commercial Ti alloys, by incorporating Ag into the coatings to introduce a bactericidal function to the surface. The Ti-30Nb-5Mo alloy, with lower elastic modulus, was treated by the MAO method using electrolyte solutions containing calcium acetate, magnesium acetate, β-glycerol phosphate, and varied concentrations of silver nitrate (1.5 mM, 2.5 mM, and 3.5 mM). With an increase in the concentration of silver ions in the electrolyte, the galvanostatic period during the MAO process decreased from 1.7 s to 0.5 s. The Ca/P ratio increased from 0.72 up to 1.36. X-ray diffraction showed that the MAO coatings were formed by rutile and anatase TiO_2 main phases and calcium phosphates. X-ray photoelectron spectroscopy analysis detected the presence of amorphous Nb_2O_5, $CaCO_3$, and $MgCO_3$, and metallic and oxide forms of Ag. The increase in Ag in the electrolyte decreased the coating thickness (from 14.2 μm down to 10.0 μm), increased the contact angle (from 37.6° up to 57.4°), and slightly increased roughness (from 0.64 μm up to 0.79 μm). The maximum inhibition of *Enterococcus faecalis*, *Pseudomonas aeruginosa*, and *Candida albicans* strains growth was of 43%, 43%, and 61%, respectively. The Ag did not negatively affect the differentiation of adipose-tissue-derived mesenchymal stem cells. Therefore, the treatment of the surface of the innovative Ti-30Nb-5Mo alloy by the MAO method was effective in producing a noncytotoxic porous coating with bactericidal properties and improved osseointegration capabilities.

Keywords: antimicrobial activity; micro-arc oxidation; silver; coating; surface modification; titanium alloy

1. Introduction

Titanium (Ti) and its alloys have a combination of mechanical, chemical, and biological properties that makes them particularly important in the medical field, especially for biomedical implants [1,2]. However, it is essential to impart biofunctional properties to their surfaces to enhance their effectiveness [3,4]. Various surface-modification treatments can be carried out to improve the surface properties of Ti alloys and make them more suitable for use as implants [5]. Chemical vapor deposition (CVD) [6], physical vapor deposition (PVD) [7,8], sol–gel [9], plasma spray [10,11], and micro-arc oxidation (MAO) [12] are among the most commonly used surface treatments of Ti alloys.

MAO is an electrochemical surface-modification method capable of producing surfaces with high corrosion and wear resistance on Ti, magnesium (Mg), and aluminum (Al) alloys [13,14]. A surface with higher porosity obtained after MAO treatment can promote high adhesion and growth of bone cells, providing better implant fixation [15–17]. Furthermore, it is a cheap and versatile method since it is possible to change several process parameters, such as substrate [5,17], electrolyte solution [18,19], voltage and current [20,21], processing time [20], and temperature [22]. By changing these parameters, it is possible to control the number and size of pores in addition to the thickness of the coatings [3]. By increasing the current and applied voltage, for example, it is possible to obtain a coating with larger pores [23–26].

An MAO coating produced on a Ti alloy substrate is composed of TiO_2. Both rutile and anatase phases can be present in the coatings, and it is possible to alter their concentrations by changing parameters during processing [27,28]; however, the higher photocatalytic activity of the anatase phase may result in a better bacterial property [29].

Another problem that can be solved by modifying Ti alloy surfaces via MAO is postoperative infection. Even following all asepsis and antisepsis protocols during the surgical procedure, microbial contamination of a wound can happen [30]. Thus, by adding antibacterial agents to the electrolyte solution of the MAO process, it is possible to produce coatings capable of fighting against microorganisms immediately after the surgical procedure [31,32]. The most commonly used elements for producing coatings with bactericidal properties are copper (Cu), zinc (Zn), and silver (Ag) [33]. Among them, Ag has the most significant potential against microorganisms [34]. This is due to the infiltration of Ag^+ ions through the bacteria's nucleic membrane, which alters and damages their DNA [33].

The Ti-30Nb-5Mo alloy is a β-metastable alloy with a body-centered cubic (bcc) crystalline structure that was recently developed. It has a higher hardness (~260 HV) and a lower elastic modulus (69 GPa) than the commercially pure Ti (CP-Ti) (164 HV and 100 GPa, respectively) and is not cytotoxic [35,36]. Its higher hardness makes the alloy more resistant to wear, and the elastic modulus closer to that of human bone (~30 GPa for cortical bone) helps to prevent the "stress shielding" effect, which can lead to loss of bone density and, consequently, to implant failure [37]. Therefore, it could represent an alternative to the use of the Ti-6Al-4V alloy since aluminum (Al) and vanadium (V) elements are considered to be toxic and harmful for the human body over the entire period of implantation [38]. Additionally, niobium (Nb) is utilized to enhance Ti alloys' corrosion resistance by forming a natural protective layer of TiO_2 and Nb_2O_5 [39,40].

The effect of Zn added to the Ti-30Nb-5Mo alloy coating has already been studied by Cardoso et al. [41]. However, a weak bactericidal effect of Zn was not enough to affect the growth of some bacteria strains on the coating's surface.

In this paper, the addition of various concentrations of Ag to the electrolyte solution containing calcium (Ca), phosphorus (P), and magnesium (Mg) was studied to produce MAO coatings on the Ti-30Nb-5Mo alloy. As a metastable β-alloy, it has a lower elastic modulus value than commercial Ti alloys. Additionally, it contains Nb, which can also be incorporated into the produced coatings, enhancing its corrosion resistance. In the present study, the surface properties and morphology of the coatings and how different concentrations of Ag affect microorganism growth on the alloy surface were investigated. X-ray diffraction (XRD) and X-ray photoelectron spectroscopy (XPS) techniques were employed

to analyze the oxide composition of the coatings. The properties of the coatings were investigated by atomic force microscopy (AFM), scanning electron microscopy (SEM), and contact angle measurements. Antimicrobial activity was investigated using *Escherichia coli*, *Staphylococcus aureus*, *Enterococcus faecalis*, *Pseudomonas aeruginosa*, and *Candida albicans*. Finally, the growth and differentiation of adipose mesenchymal stem cells (AMSCs) was also analyzed.

2. Materials and Methods

The Ti-30Nb-5Mo alloy was arc-melted in an argon-controlled atmosphere furnace. Once melted, the ingots were hot-rolled and cut to obtain 1 mm thick substrate samples measuring 10 × 10 mm^2. Finally, the samples were annealed for 6 h at 1000 °C, with a heating and cooling rate of 10 °C/min. Detailed information on this alloy's cast and bulk properties can be found in previous works [35,36,42].

The MAO process used a DC power source, Keysight, N5751A (Keysight, Santa Rosa, CA, USA). The surface-modification treatment was performed at room temperature for 60 s, applying 300 V and a limited current of 2.5 A. The electrolyte solution contained 0.35 M calcium acetate monohydrate ($(CH_3COO)_2Ca{\cdot}H_2O$), 0.02 M β-glycerol phosphate pentahydrate ($C_3H_7Na_2O_6P{\cdot}5H_2O$), 0.1 M magnesium acetate tetrahydrate ($(CH_3COO)_2Mg{\cdot}4H_2O$), and x mM (x = 1.5, 2.5, and 3.5) silver nitrate ($AgNO_3$). The concentration of all compounds was determined based on the literature analysis [17,43–45]. The samples were labeled 1.5 Ag, 2.5 Ag, and 3.5 Ag, according to the concentration of $AgNO_3$ in the electrolyte solutions.

A scanning electron microscope (SEM), model 300 FE, from Zeiss (Carl Zeiss, Oberkochen, Germany) was used to obtain images. Cross-sectional images were collected by an Olympus BX51 M optical microscope (Olympus, Tokyo, Japan). Micrographs and cross-sectional images were analyzed using the ImageJ software (version 1.53t) to obtain information on porosity, pore density, pore size, and thickness through the difference in contrast between the pores and the rest of the surface.

XRD analysis was carried out on a MiniFlex600 diffractometer (Rigaku, Tokyo, Japan). The data were collected using Cu Kα radiation and 10°/min collection time (0.04° steps). XPS data were collected using a spectrometer, Phoibos 100-MCD5 from SPECS (SPECS, Berlin, Germany), with an AlKa (1486.6 eV) achromatic radiation source. The instrument was operated in FAT mode at 100 W. A channel width of 1 eV was used for wide regions, and 0.1 eV for high-definition regions. The CasaXPS software (version 2.3.25) was used to calculate the composition of each element based on the peak intensities.

Contact angle measurements with deionized water were performed on an HTM Reetz GmbH goniometer (HTM Reetz GmbH, Berlin, Germany). The wettability of the samples was determined using the droplet technique. Three drops were deposited on each sample for statistical calculations. AFM images were obtained in noncontact mode using an XE-120 microscope (Park, Suwon, Republic of Korea), with two 30 × 30 μm^2 images taken to assess surface roughness.

In order to test the microorganism growth on the substrate and coatings, four different bacteria strains (*S. aureus*, *E. coli*, *P. aeruginosa*, and *E. faecalis*), along with the *C. albicans* fungus, were used. Before testing, all the samples underwent sterilization by autoclaving at a temperature of 121 °C for a duration of 20 min. Subsequently, each sample was transferred into individual tubes. In each of these tubes, a suspension of a single microorganism, previously prepared using 5 mL of Brain Heart Infusion solution (BHI, DIFCO, Sparks, NV, USA), was added. All tests were conducted three times to ensure accuracy and reliability of the results. A BHI medium with no samples was used as the control. Every microorganism was cultivated at its optimal growth temperature (28 °C for fungus and 37 °C for bacteria) with slow agitation for 24 h. A biophotometer (Eppendorf, Hamburg, Germany) was employed to measure the optical density at a wavelength of 600 nm to assess the growth of microorganisms.

For cell tests, adipose mesenchymal stem cells (AMSC) were employed. The AMSCs were extracted from the adipose tissue of 3-month-old female lambs obtained from a local slaughterhouse. The cells were incubated with substrates for 24 h, followed by the addition of MTT solution (3-[4,5-dimethylthiazol-2-yl]-2,5-diphenyl-tetrazolium bromide, Sigma-Aldrich, Gillingham, UK) to the DMEM medium (Gibco, Loughborough, UK) containing 10% Fetal Calf Serum (FCS, Gibco, Loughborough, UK). The solution with the AMSCs was subjected to a controlled environment at 37 °C with 5% CO_2 for a period of 3 h. Following this incubation, the culture medium was removed, and absolute ethanol (Sigma-Aldrich, Gillingham, UK) was added to replace the MTT solution. This test is based on the reduction in MTT, a yellow tetrazolium salt, to insoluble purple formazan crystals by metabolically active cells. This reaction occurs predominantly in the mitochondria and has been used to determine the cytotoxicity of substances potentially toxic to AMSCs. The solubilized formazan was measured at 600 nm using a biophotometer (Eppendorf, Hamburg, Germany).

To analyze osteogenic differentiation capacity, the AMSCs were subjected to a three-week treatment with DMEM medium that contained 10% FCS supplemented with 50 µg/mL ascorbic acid, 10 mM ß-glycerophosphate, and 10^7 M dexamethasone. Subsequently, the cells underwent treatment with ethanol (70%) for 1 h at room temperature and were washed with distilled water to fix them. Following this, the cells were thoroughly rinsed with distilled water to eliminate any residual ethanol. Afterward, the cells underwent a staining process using a 2% solution of Alizarin Red S (Carlo Erba, Cornaredo, Italy) for 30 min. The purpose of this staining was to identify the presence of calcium deposits within the cells.

One-way analysis of variance (ANOVA) was used to identify statistically significant differences and performed using the OriginPro® 8.5 software. Statistical significance was defined as * ($p < 0.05$), ** ($p < 0.01$), and *** ($p < 0.001$).

3. Results and Discussion

During the MAO process, the current of the circuit was monitored. Figure 1 presents the time dependence of current obtained during the MAO process for the 1.5 Ag, 2.5 Ag, and 3.5 Ag samples. The typical behavior of current versus time can be separated into two main stages during the growth of the ceramic coating, and the first stage is highlighted in Figure 1. During the MAO process, the current was limited to 2.5 A and remained at this value during the galvanostatic stage. In this first stage, the oxide coating was growing and did not have enough electrical resistance to break the dielectric barrier [46]. When the potential reached a critical value, the dielectric barrier was broken (points highlighted in Figure 1), and the current began to decrease (potentiostatic stage), tending to a constant value in the final phase of the process. During the galvanostatic process, the electric arcs had the highest energy, increasing the coating's thickness and incorporating the electrolyte elements into the coating. After breaking the dielectric barrier, the number of micro-arcs on the sample's surface decreased [17,46].

For the 1.5 Ag, 2.5 Ag, and 3.5 Ag samples, the dielectric barrier breakdown occurred after 1.7 s, 1.2 s, and 0.5 s, respectively. Thus, the increase in the ions concentration in the electrolyte reduced the time of the galvanostatic stage. This occurred because, with the increase in the ions' concentration, the solution conductivity also increased, which led to the increase in the process energy, facilitating the coating growth and, consequently, breaking the dielectric barrier more quickly. The same phenomenon was observed by Wang et al. [47], who increased the concentration of $NaPO_3$ in the electrolyte and, consequently, the time for dielectric breakdown decreased.

Figure 2 shows the SEM images of the samples after MAO treatment with different electrolyte solutions, varying the Ag concentration. It is possible to visualize the typical morphology of surfaces oxidized by MAO, containing pores of different dimensions in the shape of volcanoes. Small differences between the images can be observed, except for small cracks that appear in the coating of the 3.5 Ag sample. The appearance of cracks may be

associated with the increase in process energy due to the increase in the amount of ions in the electrolyte. With the increase in energy, the temperature during the MAO process also increased, which can cause cracks in the ceramic coating due to the difference between the coefficient of thermal expansion of the ceramic (coating) and the metal (substrate) [48].

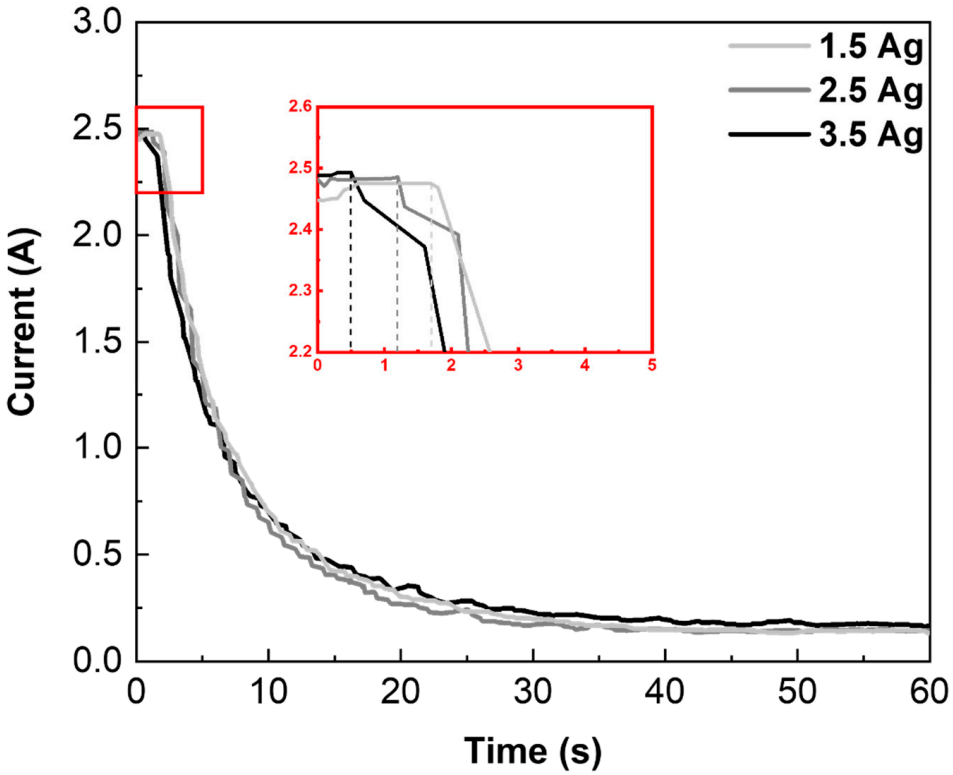

Figure 1. Current–time curves recorded during the MAO process for the different Ag concentrations.

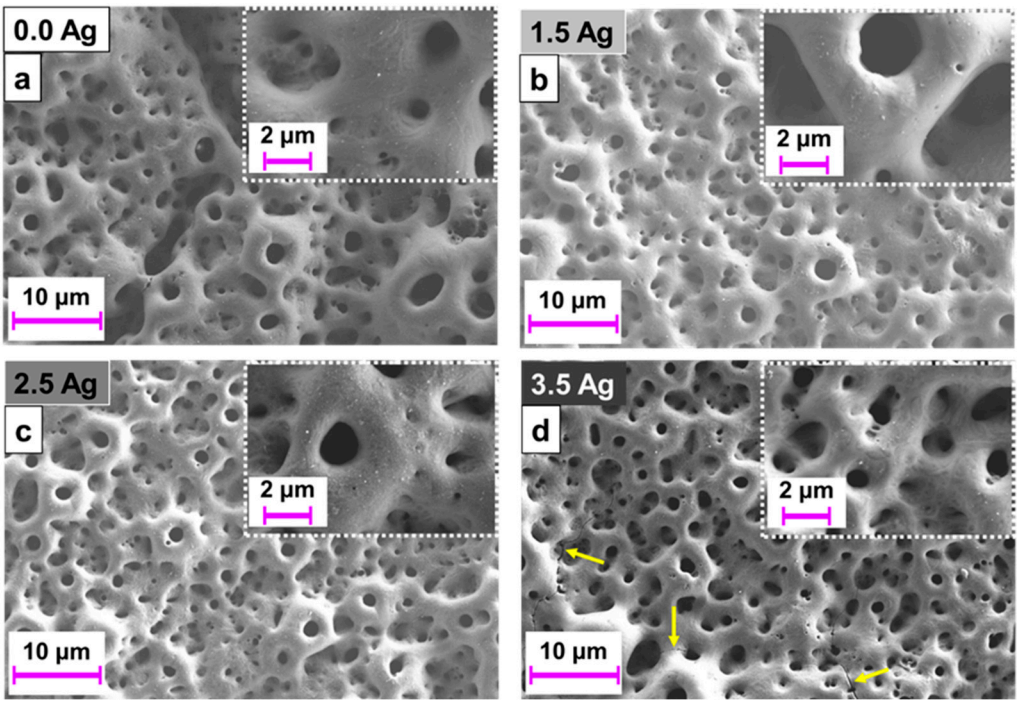

Figure 2. SEM images of the 0.0 Ag (**a**), 1.5 Ag (**b**), 2.5 Ag (**c**), and 3.5 Ag (**d**) samples' surfaces after MAO treatment: the larger squares correspond to 2k× magnification, and the smaller ones to 10k× magnification.

Figure 3 displays the information obtained from the ImageJ software (version 1.53t) regarding the sample surfaces' porosity and pore density (number of pores/area). There was no observable trend in the plotted curves, indicating that an increase in Ag in the electrolyte solution did not significantly affect the variation in porosity and pore density of the formed coatings ($p > 0.05$).

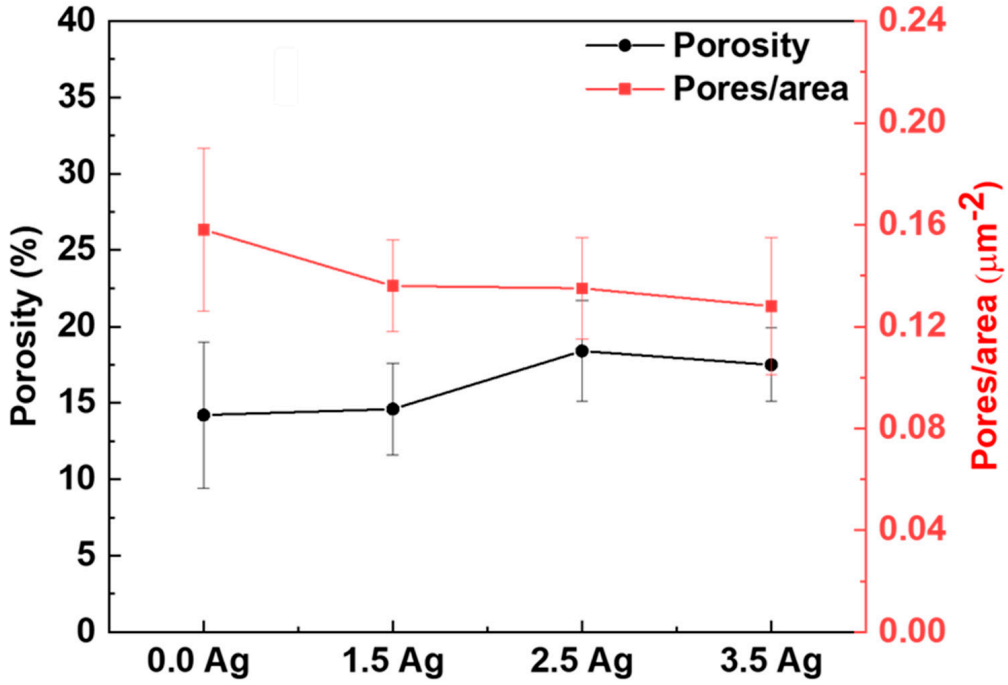

Figure 3. Porosity and pore density of the MAO coatings with various Ag concentration.

The XRD patterns of the samples after the MAO incorporating Ag are shown in Figure 4. Peaks from the anatase and rutile phases of TiO_2 were detected in all samples. Furthermore, calcium phosphate peaks were detected in the 1.5 Ag and 2.5 Ag samples. Cardoso et al. [41] presented the results of the MAO process in the Ti-30Nb-5Mo alloy using the same electrolyte, but without $AgNO_3$. Their results showed that the crystalline part of the Ag-free coating is composed only of TiO_2 (65% anatase and 35% rutile).

Figure 5 presents the proportion of each phase detected by the XRD, calculated using Equation (1) [49], which considers the relative intensity of each peak. There was an increase in the rutile phase, compared to the coating without Ag [41], due to the increase in the energy of the process.

$$\%\text{phase} = \frac{\sum I_{\text{phase}}}{\sum I_{\text{all phase}}} \quad (1)$$

TiO_2 can exist in three crystalline phases: anatase, rutile, and brookite. The anatase phase is the easiest to form as it requires low temperatures to become stable. Above 600 °C, there is sufficient energy for the rutile phase to be formed [50,51]. Therefore, due to the extremely high temperature during the formation of arcs in the MAO process [52,53], there is enough energy to stabilize both the anatase and rutile phases of TiO_2.

To calculate the crystallinity of the samples, each diffraction pattern was decomposed in the OriginPro® 8.5 software, obtaining an area of amorphous halo (Aa) and another area of crystalline peaks (Ac). Thus, crystallinity was calculated using Equation (2) [54].

$$\text{crystallinity} = \frac{A_c}{A_T} \times 100 \quad (2)$$

where A_T is a total area ($A_c + A_a$) [54].

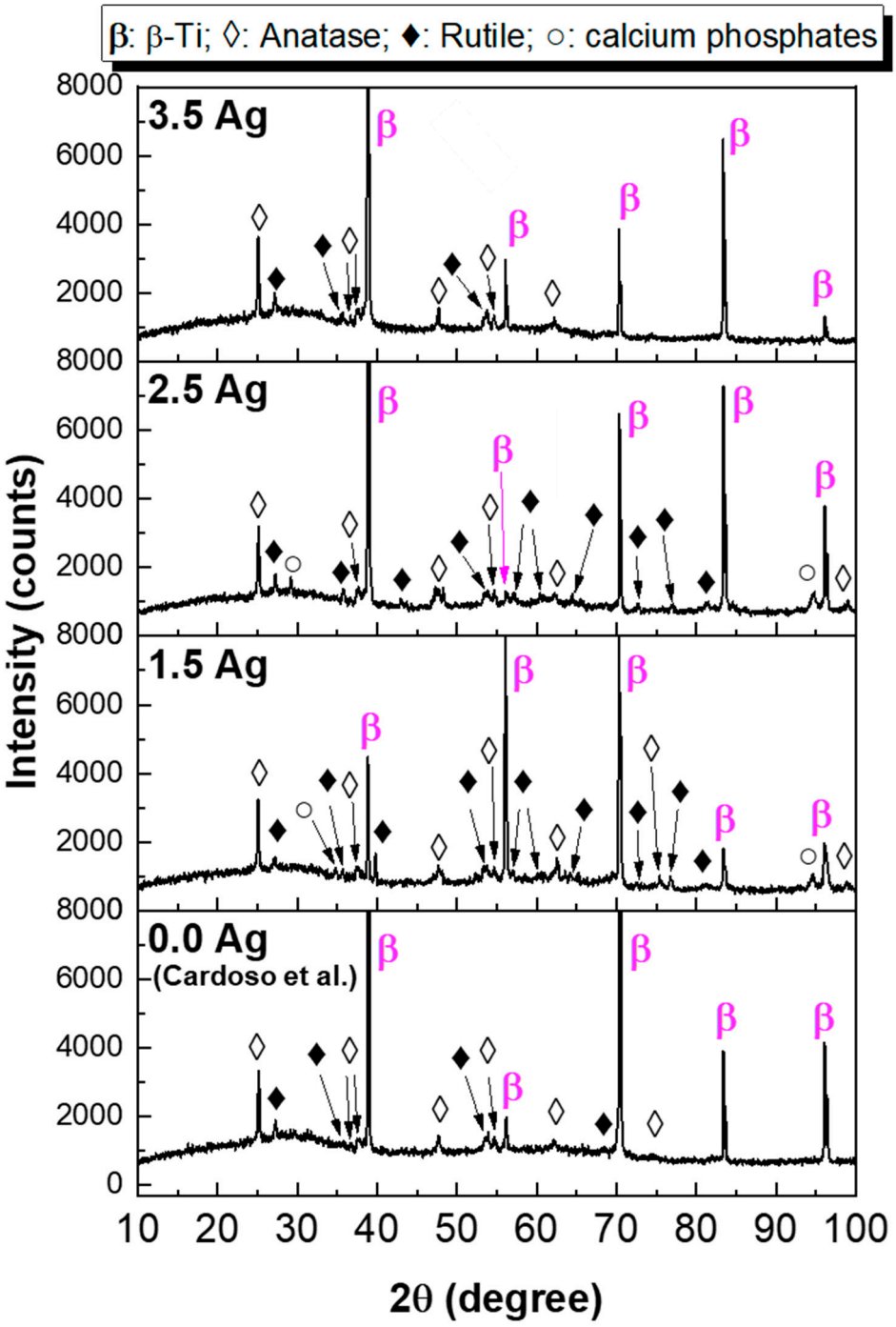

Figure 4. XRD profiles of the MAO surfaces with different Ag concentration [41].

Figure 5 also shows the crystallinity of each coating. There was no significant variation in the crystallinity between the coatings of the 1.5 Ag and 2.5 Ag samples, and the values were maintained between 29% and 30%. However, due to the absence of crystalline calcium phosphates in the 3.5 Ag coating, the crystallinity of this sample decreased to 17%. As mentioned earlier, the temperature during the MAO process is very high (~2000 K). Furthermore, after the process is complete, the cooling rate is also high due to the electrolytic bath in which the sample is immersed [46,53]. Therefore, the ceramic coating produced by the MAO process tends to be predominantly amorphous [48,55,56].

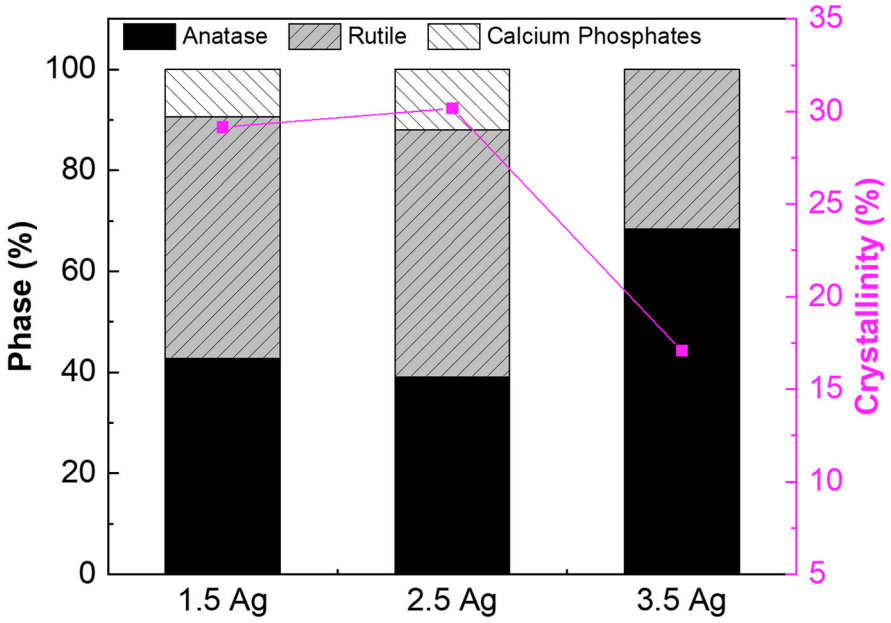

Figure 5. Crystallinity and phase composition of the MAO surfaces with different Ag concentration.

The low crystallinity also helps to explain why the percentage of the rutile phase is lower in the 3.5 Ag sample. With increasing energy, the amount of rutile should increase. However, the increase in energy also increases the cooling rate of the coating, increasing the amorphous phase. Thus, most of the rutile phase is probable in the amorphous phase, reducing its quantity in Figure 5.

Figure 6 represents the cross-section of the samples, with the thickness of each coating displayed in the images. There was a slight increase in the thickness between the 0.0 Ag and 1.5 Ag samples. However, no significant difference was observed between the 1.5 Ag and 2.5 Ag samples, while the 3.5 Ag coating was thinner than the others. Although MAO coating growth can occur throughout the process, it is during the galvanostatic stage that this occurs most rapidly [17,46]. Based on Figure 1, it can be observed that the galvanostatic period of the 3.5 Ag sample was less than half the time of the other samples. Consequently, the remaining process time was insufficient for the 3.5 Ag coating to reach the same thickness as the other two coatings. Zhang et al. [57] varied the Ag concentration in the MAO electrolyte performed on CP-Ti samples. Their results also showed no significant difference in thickness between the coatings, but a slight decreasing trend was observed in samples with higher amounts of Ag.

In Figure 6d, a dark line between the substrate and the coating can be noticed. This may indicate a coating peeling due to the preparation process for obtaining images and could suggest a possible lower adhesion between the coating and the substrate. Further analysis should be carried out in the future to understand this characteristic. Therefore, considering that the black line may indicate low adhesion of the coating, the 1.5 Ag sample shows higher adhesion with the substrate.

Since most of the coatings were composed of amorphous materials, Figure 7 displays the high-resolution XPS spectra of the alloying elements (Ti, Nb, and Mo) and those incorporated during the MAO process (Ca, P, Mg, O, C, and Ag), to analyze phases that were not detected by XRD. Upon Ca spectrum deconvolution, peaks corresponding to the $CaCO_3$ doublet appeared at 347.2 eV and 350.7 eV [45,58,59]. For P, at 133 eV, the spectrum showed a $(PO_4)^{3-}$ phosphate peak [45,59–61]. According to the Mg high-resolution spectrum analysis, the peak for $MgCO_3$ was observed at 1305 eV [45]. Regarding the alloying elements, the TiO_2 doublet was observed, with peaks at 458.5 eV and 464.1 eV [45,46,59,61,62], the Nb_2O_5 peaks of the 3d, $3d_{5/2}$, and $3d_{3/2}$ doublets were observed at 207.1 eV and 209.8 eV [46], and no peaks of Mo were detected. In addition to the low concentration of Mo in the

substrate alloy, its property as a valve metal makes its oxidation less energetically favorable by the MAO method [41,63]. The Ag peaks ($3d_{3/2}$ and $3d_{5/2}$) can be deconvoluted into two doublets. The 368.4 eV and 374.4 eV peaks correspond to the metallic Ag [64,65], and the doublet at 365.7 eV and 373.8 eV correspond to Ag 3d in the Ag_2O form [65,66]. Contamination by C occurs due to the use of acetates, resulting in peaks of C–C, C–O–C, and O–C=O bonds at 284.8 eV, 286.2 eV, and 290.0 eV, respectively, in the C1s spectrum [61,67]. Finally, the O1s spectrum exhibited peaks at 531.5 eV for metallic oxides and 533.6 eV for hydroxide (OH) [59].

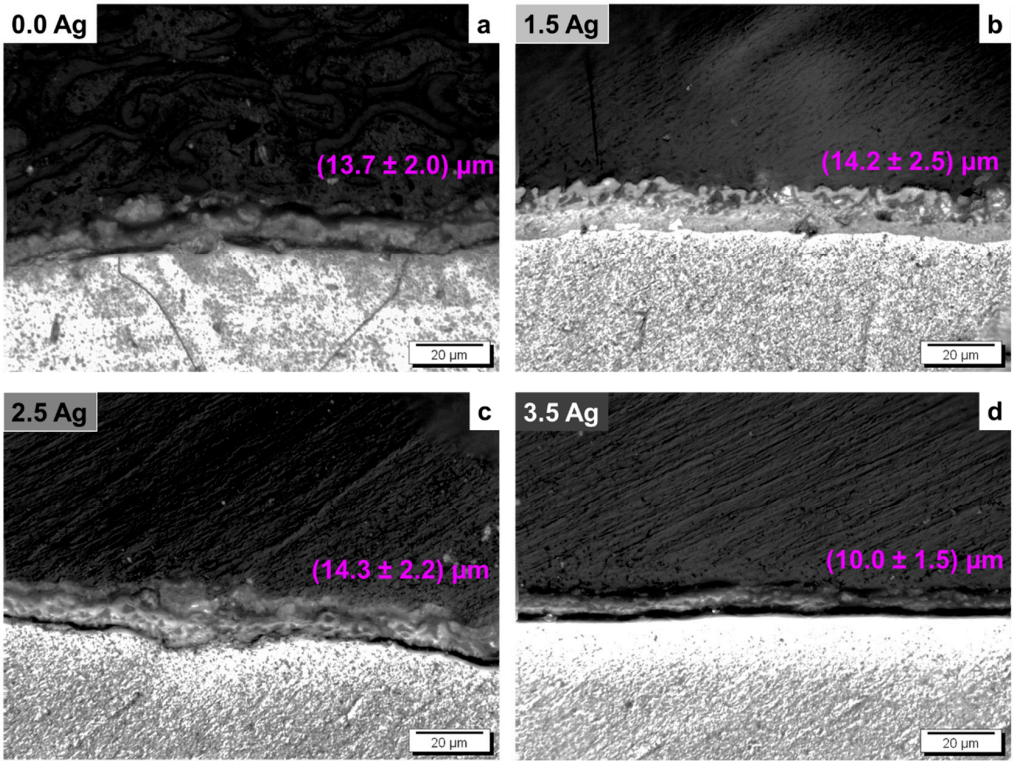

Figure 6. Cross-section images of the 0.0 Ag (**a**), 1.5 Ag (**b**), 2.5 Ag (**c**), and 3.5 Ag (**d**) samples.

From the spectra in Figure 7g, it can be observed that Ag is present primarily in the metallic form, not in the Ag^+ state. It is known that $AgNO_3$ decomposes into metallic Ag with temperature according to the following reduction reaction [68]:

$$2AgNO_3 \xrightarrow{\Delta} 2Ag + 2NO_2 + O_2$$

The composition of the elements identified by the XPS analysis is illustrated in Figure 8. In Figure 8a, the compositions of the elements Mg, Ti, Nb, and Ag are presented, and in Figure 8b, the compositions of the elements Ca, P, C, and O, along with the Ca/P ratio for each sample are shown. The amount of Ti and O in the coatings decreased, while the portion of C increased with higher concentrations of Ag ions in the electrolyte solution. The concentration of P in the coatings decreased, while the amount of Ca remained practically unchanged, resulting in a gradual increase in the Ca/P ratio. Zhang et al. [55] studied the variation of Zn composition in the electrolyte to produce coatings on the Ti-6Al-4V alloy. In [55], the authors showed that the Ca/P ratio of the coatings also increased with rising Zn^{2+} concentration in the electrolyte. Therefore, they predicted that by increasing the amount of Zn, values close to the ideal hydroxyapatite (HA) value (1.67) could be reached [53]. Thus, it was speculated that the Ca/P ratio may also increase to values close to 1.67, with the increase in the concentration of Ag ions in the electrolyte. However,

increasing Ag should be performed cautiously since high levels of this element in the coating can make it cytotoxic [33].

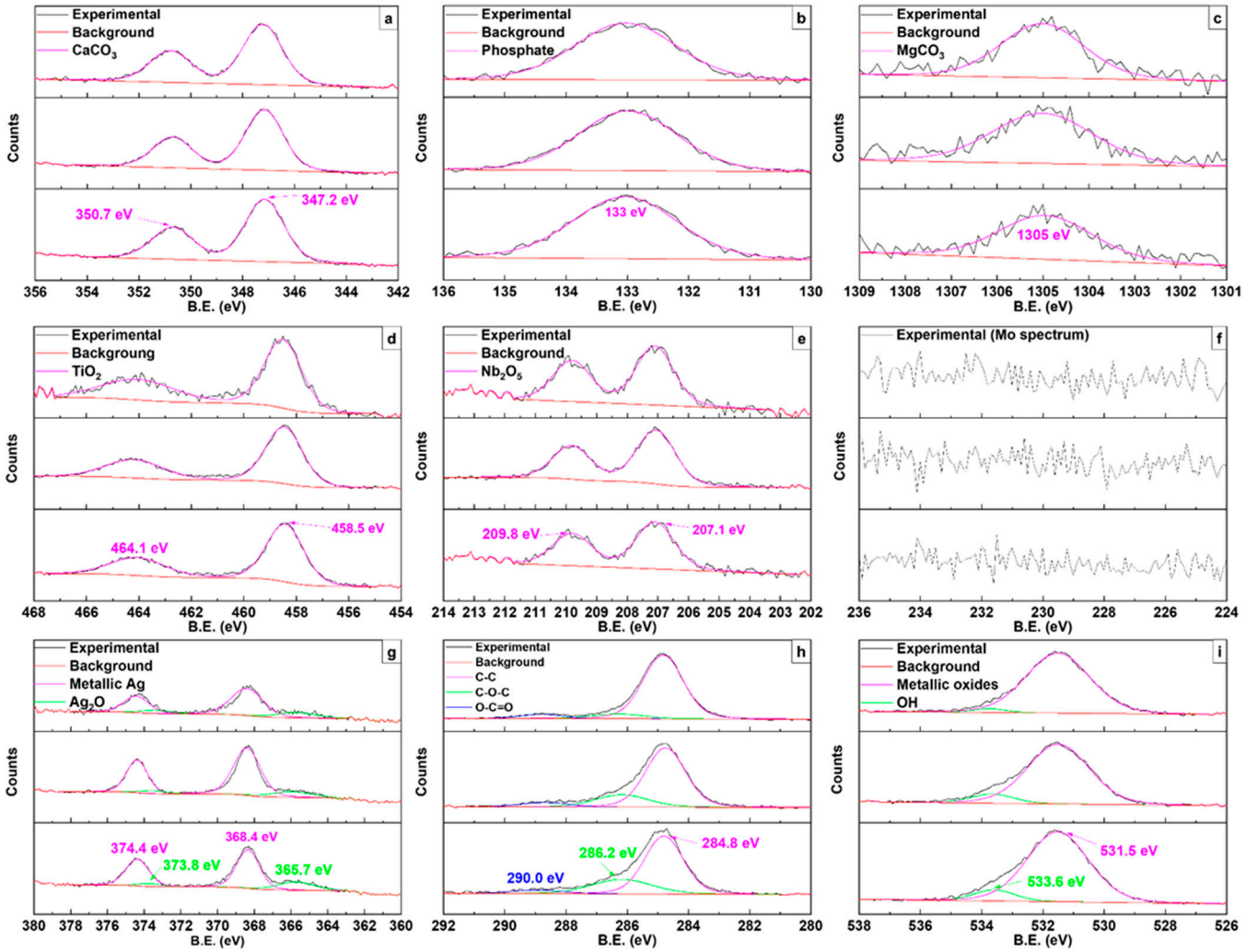

Figure 7. High-resolution XPS of the Ca (**a**), P (**b**), Mg (**c**), Ti (**d**), Nb (**e**), Mo (**f**), Ag (**g**), C (**h**), and O (**i**) in the MAO surfaces.

A more significant increase in the amount of Ag in the coating was anticipated compared to the observed result, as a higher concentration of $AgNO_3$ in the electrolyte typically results in a greater availability of Ag ions for incorporation. In fact, the 3.5 Ag sample had a lower Ag content than the 2.5 Ag sample. This can be explained by the decrease in the galvanostatic period. Figure 1 shows that the galvanostatic period of the 3.5 Ag sample was the shortest of all, and it is known that during this stage, the highest incorporation of the electrolyte elements into the coating occurs [46].

Figure 9 presents the 3D images of the coatings' topography obtained by AFM. As in the SEM images (Figure 2), it is possible to observe a typical morphology of MAO coatings containing micropores. The average roughness values (RMS) of each sample are shown in the graph in Figure 10. It was observed that a higher concentration of $AgNO_3$ in the electrolyte led to a slight increase in the roughness of the coatings ($p < 0.001$). This is because the number of conducting ions in the electrolyte solution increased, leading to a rise in energy during the MAO process [3,41,69]. The cracks in the coatings can also led to the roughness [48].

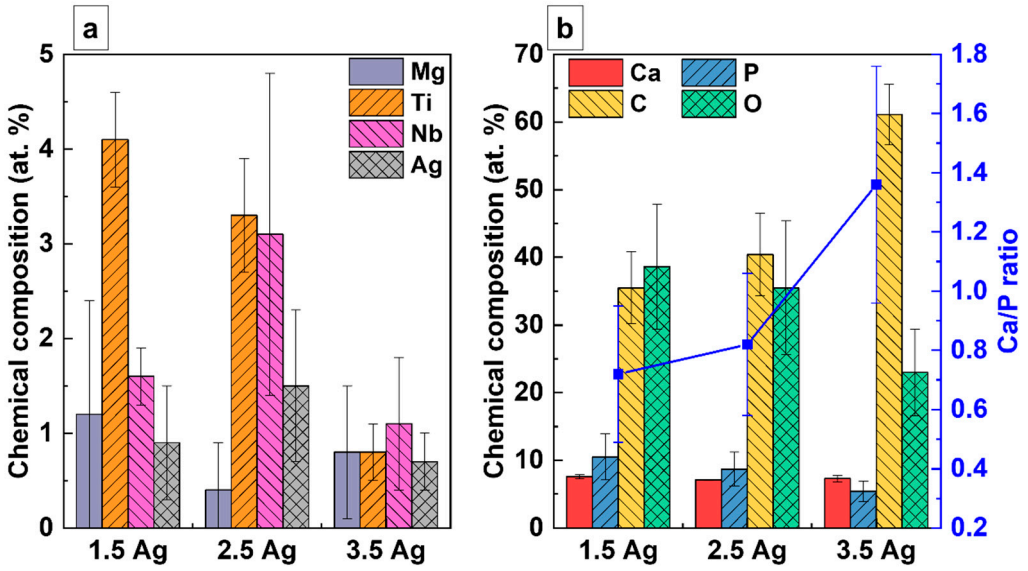

Figure 8. (**a**,**b**) Chemical composition obtained by XPS of the MAO coatings.

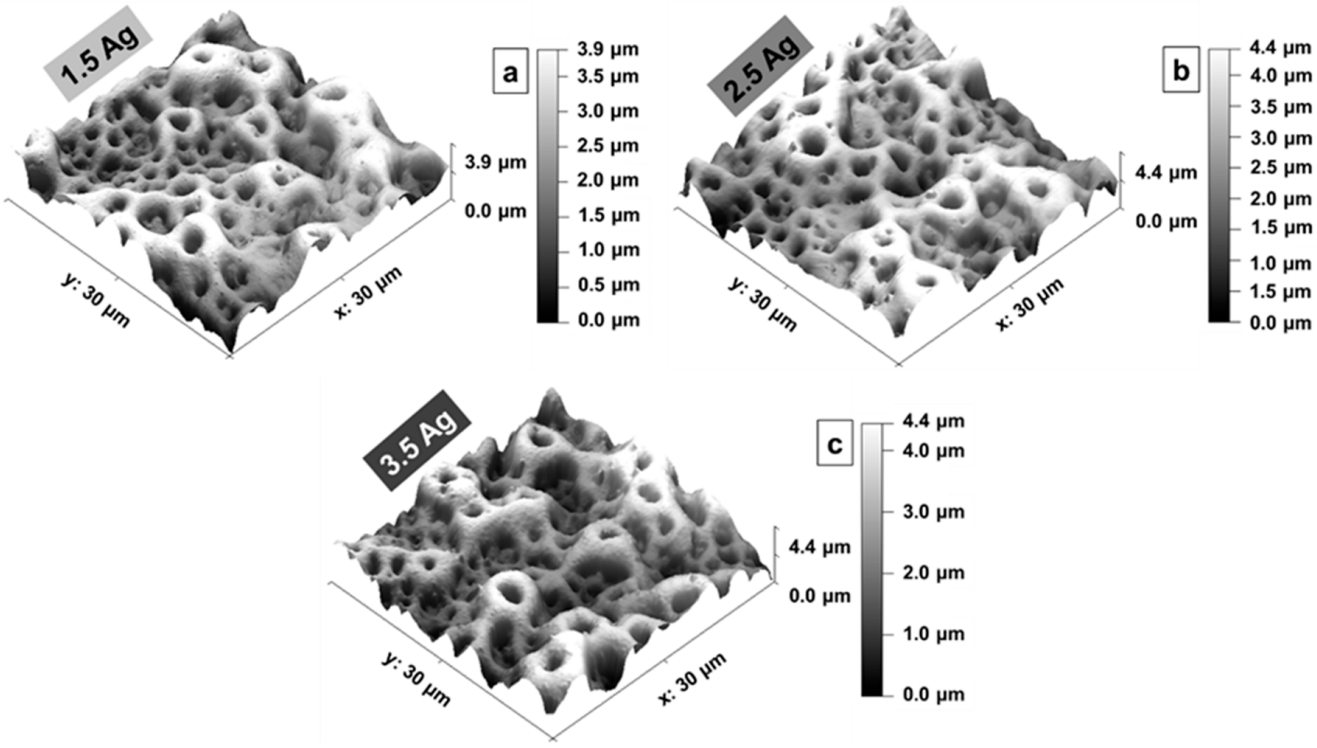

Figure 9. 3D topography images of the 1.5 Ag (**a**), 2.5 Ag (**b**), and 3.5 Ag (**c**) samples.

Figure 11 shows that the contact angle of the samples' surface with distilled water increased proportionally to the amount of Ag in the electrolyte. Despite the increase, all the coatings had a contact angle lower than 90° and, therefore, were hydrophilic. The MAO coatings containing TiO_2 with a high surface polarity, easily binding with water molecules, are characterized by hydrophilic character [17,48,70]. However, the appearance of cracks in the coatings led to an increase in the contact angle. According to Chu et al. [71], cracks can create air pockets due to the retention of atmospheric air, which increases the contact angle of the surface.

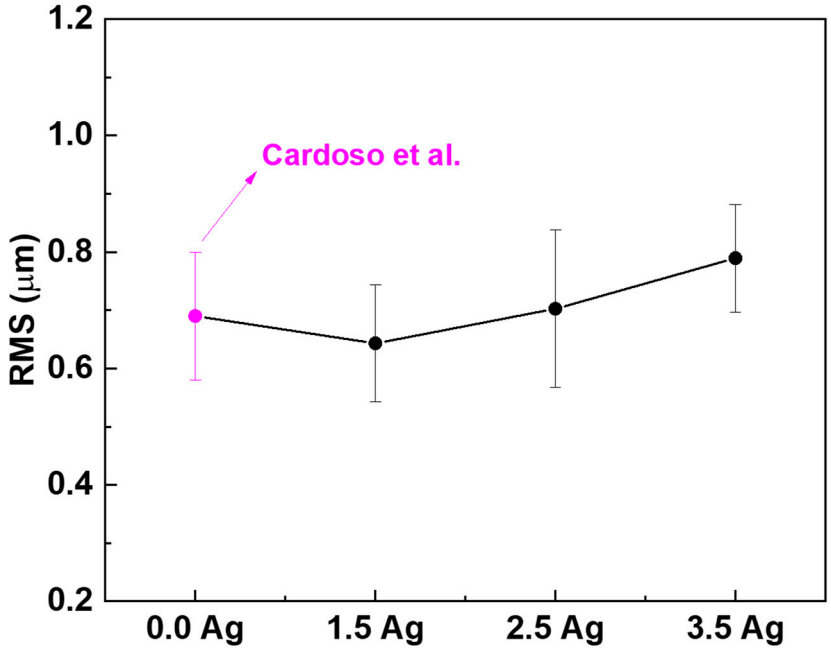

Figure 10. Roughness of the MAO surfaces [41].

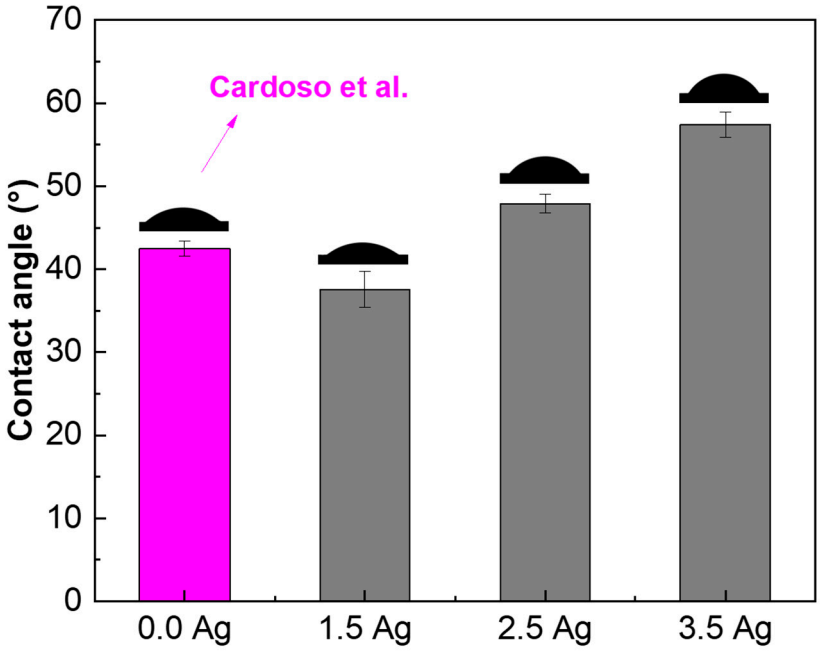

Figure 11. Contact angle of the MAO coatings with different Ag concentration [41].

Figure 12 shows the results of the microorganisms' growth (*E. coli*, *S. aureus*, *E. faecalis*, *P. aeruginosa*, and *C. albicans*) in samples containing Ag. The BHI medium without samples was used as the control group. The comparison with the sample without Ag was performed with the data from Cardoso et al.'s [41] study. There was no significant difference in the growth of *E. coli* and *S. aureus* compared to the control for any sample, but a slight decrease in *S. aureus* growth was observed with the increase in the Ag concentration (from 99% down to 94% growth). Analyzing the growth of the other bacteria strains (*E. faecalis* and *P. aeruginosa*), their significant decrease was observed when incorporating Ag into the coating of all samples. The growth of *E. faecalis* was 61%, 60%, and 57%, while for *P. aeruginosa*, it was 57%, 63%, and 63%, on the 1.5 Ag, 2.5 Ag, and 3.5 Ag samples,

respectively. Finally, for the 1.5 Ag and 2.5 Ag samples, a significant reduction in the *C. albicans*' fungus growth was registered (by 61% and 58%, respectively). The decrease in the fungus growth was also significant for the 3.5 Ag sample compared to the control (by 14%). However, there was an increase when compared to the 2.5 Ag sample.

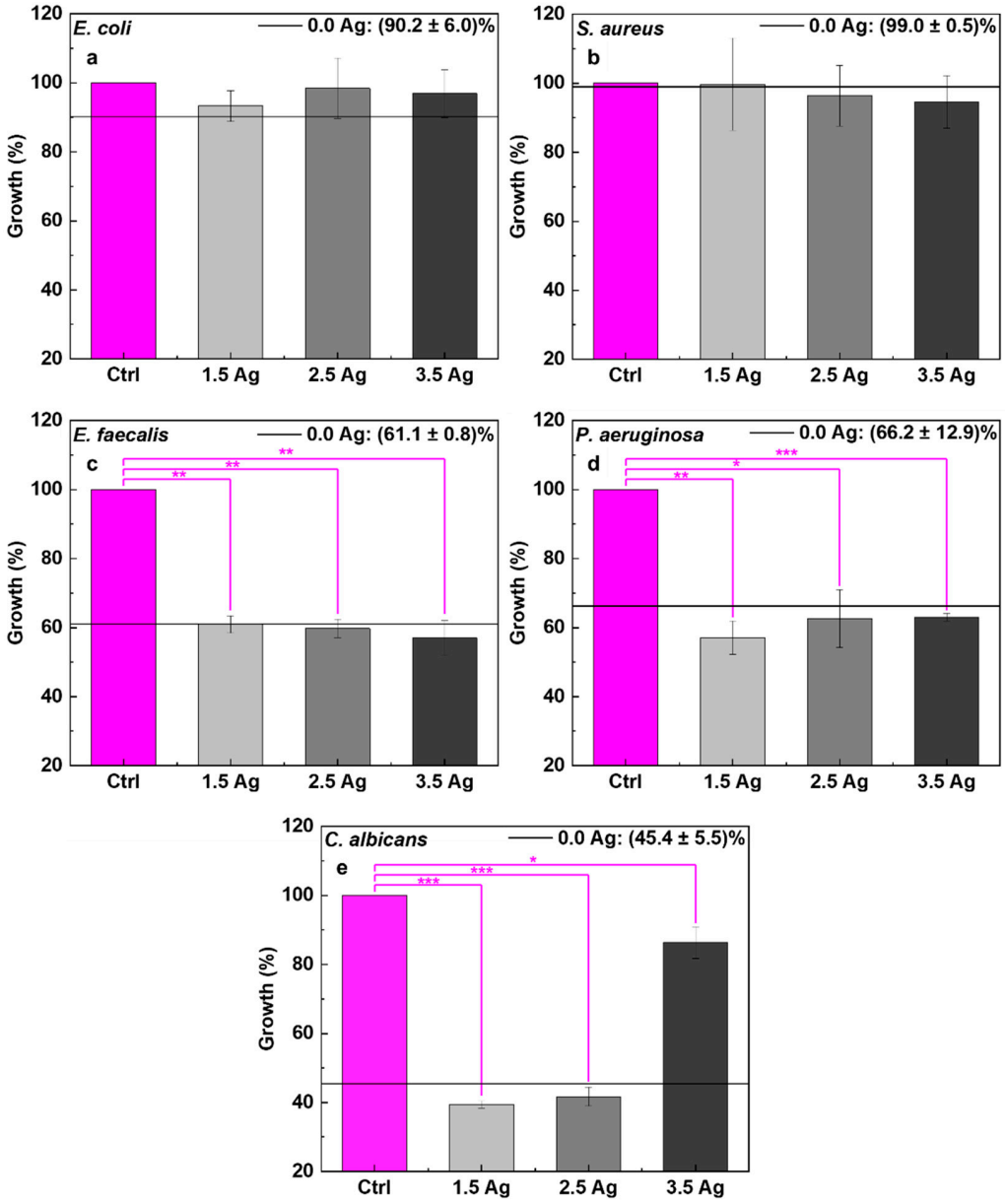

Figure 12. *E. coli* (**a**), *S. aureus* (**b**), *E. faecalis* (**c**), *P. aeruginosa* (**d**), and *C. albicans* (**e**) growth on the MAO surfaces (* $p < 0.05$, ** $p < 0.01$, and *** $p < 0.001$, compared with the control group).

Although the obtained results were expected for most of the prepared samples, an unusual growth of microorganisms in some cases was observed. This happened likely due to other factors affecting the microbial growth on the MAO coatings (beyond the presence of bactericidal elements). The pH, temperature, the presence of other chemical compounds, wettability, and, especially, the coatings' roughness, can influence microorganisms' adhesion to the surface. Figures 11 and 12 demonstrated that all samples exhibit hydrophilic properties, and that the roughness of the coatings increased for those containing with higher amounts of Ag. Although hydrophilicity and roughness are important factors for cell adhesion to the material's surface, they also make the surface of the samples a favorable environment for the growth of bacterial colonies [72–74]. Another factor can be a nonhomo-

geneous presence of Ag in the coatings (as follows from the XPS results), creating regions without impediments to microbial growth on the sample surface. Increasing the MAO process time could overcome this problem, allowing a more homogeneous incorporation of the elements.

Another factor that should be considered is in which form Ag is incorporated into the MAO coatings (for example, as Ag nanoparticles (AgNPs), oxide Ag, metallic Ag, etc.). It is known that AgNPs have an extremely high bactericidal effect when they are on the surface of the coating [75]. However, the Ag contained in the samples prepared in this current study was incorporated into the TiO_2 coating. This made Ag release highly dependent on the interaction of the coating with the medium around it [76]. In other words, the bactericidal action of the coating depends on the capacity of water to interact and penetrate the porous surface [33]. The wettability results obtained in this work showed that the contact angle of the MAO surfaces increases with the addition of Ag. This causes the interaction between the TiO_2 coating and the bacteria membranes to be relatively smaller, reducing the release of Ag. For *E. faecalis* and *P. aeruginosa*, this decrease in Ag release had no significant effect. However, the decrease in effectiveness was noticeable for the *C. albicans* fungus since the sample with greater Ag incorporation showed higher microbial growth compared to the others with less Ag.

Figure 13 shows the AMSCs' growth results obtained by the MTT method. The control group tests were performed by growing the AMSCs without any samples, and the results were also compared to the coating without Ag [41]. As the concentration of Ag increased, the growth of AMSCs somewhat decreased, likely due to some cytotoxicity of Ag [33,64,77]. Therefore, controlling the concentration of Ag in materials is important to prevent cell death. Regardless, the cell growth in all samples was above 70%: 98%, 92%, and 87% for the 1.5 Ag, 2.5 Ag, and 3.5 Ag samples, respectively. The ISO 10993-5 standard [78] established that a sample is considered cytotoxic when the cell culture viability is less than 70% [79–81]. Therefore, none of the tested samples was cytotoxic, according to the ISO 10993-5 standard. It is worth mentioning that the registered trend indicates that the amount of Ag should be carefully controlled, and in the case of a further increase in Ag concentration, the samples can become cytotoxic for the AMSCs.

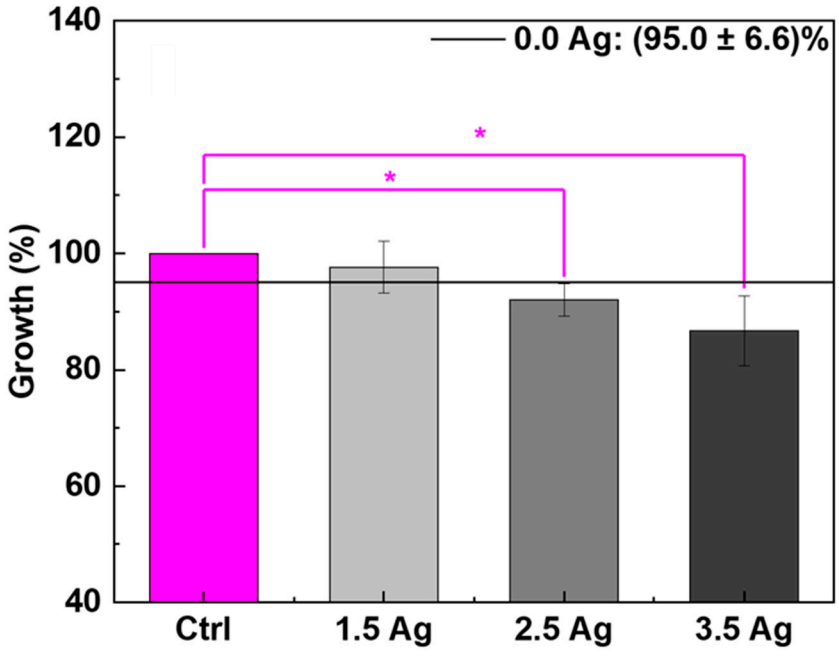

Figure 13. AMSCs' growth on the MAO coatings with different Ag concentration (* $p < 0.05$, compared with the control group).

Figure 14 shows the images of cell monolayers in all the samples, which were stained with Alizarin Red S to highlight calcium deposits in red. The positive control (+Ctrl) consists of AMSCs that have differentiated into the osteogenic lineage without the substrate, and the negative control (−Ctrl) is represented by nondifferentiated AMSCs. All the images are similar to the positive control. Therefore, small amounts of Ag in the samples developed in this work did not affect the differentiation of AMSC into the osteogenic lineage. However, higher concentrations of Ag may negatively interfere with the process. Cardoso et al. [41] showed that the same results were obtained with the coating without Ag. Shimabukuro et al. [82] studied the addition of $AgNO_3$ to the electrolyte during the MAO treatment of CP-Ti and also demonstrated that adding small amounts of Ag did not alter the differentiation of MC3T3-E1 cells.

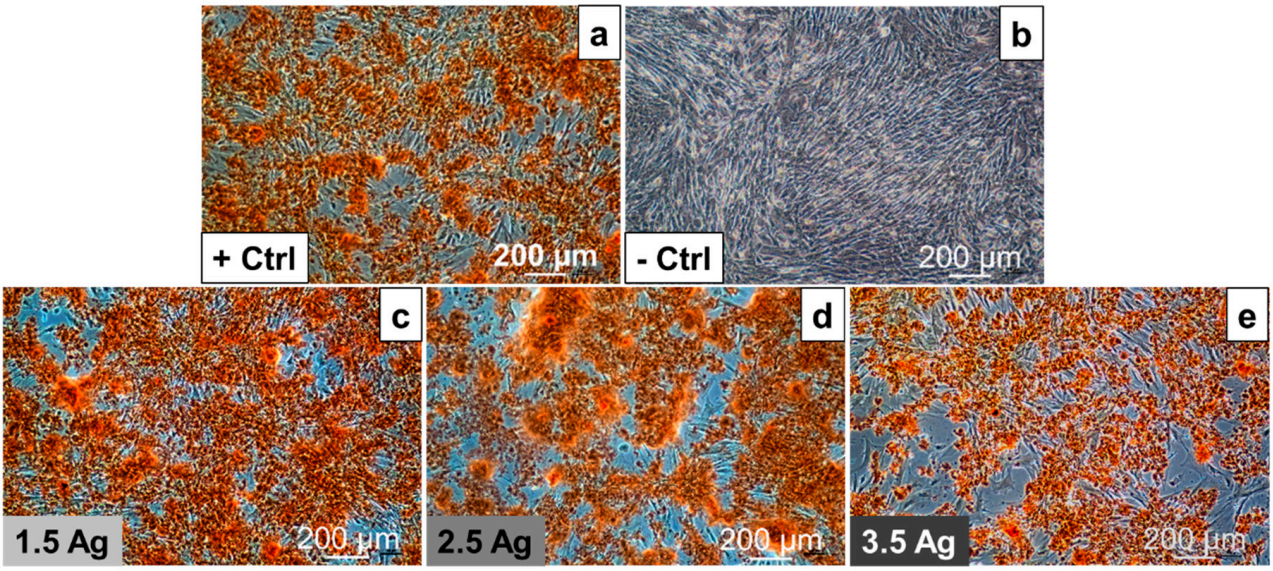

Figure 14. Alizarin Red S staining of AMSCs differentiated in vitro into the osteogenic lineage on positive control (**a**), negative control (**b**), and 1.5 Ag (**c**), 2.5 Ag (**d**), and 3.5 Ag (**e**) coating samples.

4. Conclusions

The present study demonstrated that the energy of the MAO process increased with an increasing concentration of Ag ions from 1.5 mM to 3.5 mM.

The XRD analysis indicated that the coating's crystalline main phase consisted of TiO_2 (anatase and rutile) and calcium phosphates. The XPS spectra revealed that the coatings contained both metallic Ag and Ag_2O. The Ca/P ratio of the coatings increased from 0.72 to 1.36 when more Ag was added to the electrolyte, indicating that the value of 1.67 can be reached if the Ag concentration is increased.

There was an increase in the coatings' roughness (from 0.64 µm to 0.79 µm) and contact angle (from 37.6° up to 57.4°), but all the samples remained hydrophilic (<90°).

The addition of Ag in the coatings reduced the growth of *E. faecalis* by approximately 40% for the 3.5 Ag sample, and of *P. aeruginosa* by approximately 40% for the 1.5 Ag sample, as well as of the fungus *C. albicans* by approximately 60% for the 1.5 Ag sample.

Cell growth values were above 80% for all coatings produced, indicating that the coatings are not cytotoxic, and the addition of Ag did not affect the differentiation of AMSCs into osteogenic lineage. Hence, the MAO treatment effectively modified the surface of the Ti-30Nb-5Mo alloy and produced noncytotoxic porous coatings that inhibited microorganism growth and promoted better osseointegration.

Based on the results, the 1.5 Ag sample coating presented better characteristics for use in biomedical and bactericidal materials.

Author Contributions: Conceptualization, G.C.C.; methodology, G.C.C., K.B., P.A.B.K., A.D.B., R.T., I.A. and V.M.; formal analysis, G.C.C., K.B., P.A.B.K., A.D.B., R.T. and I.A.; investigation, G.C.C., K.B., P.A.B.K., L.I., M.O., A.D.B. and R.T.; resources, C.R.G. and J.V.R.; data curation, G.C.C., K.B. and P.A.B.K.; writing—original draft preparation, G.C.C.; writing—review and editing, C.R.G. and J.V.R.; supervision, C.R.G. and J.V.R.; project administration, C.R.G. and J.V.R.; funding acquisition, C.R.G. and J.V.R. All authors have read and agreed to the published version of the manuscript.

Funding: This research was funded by Coordenação de Aperfeiçoamento de Pessoal de Nível Superior—Brazil (CAPES) (grant #88887.716787/2022-00) and Conselho Nacional de Desenvolvimento Científico e Tecnológico (CNPq) (Grant #314.810/2021-8). The present research was partially supported by the Italian Ministry of Health, grant codes IZS LT 02/21 RC and IZS LT 10/22 RC.

Institutional Review Board Statement: Not applicable since adipose tissue derived mesenchymal stem cells were isolated from the adipose tissue of 3-month-old female lambs taken at the slaughterhouse.

Informed Consent Statement: Not applicable.

Data Availability Statement: The obtained data are available upon a reasonable request to the corresponding author.

Acknowledgments: The authors thank Fenelon Martinho Lima Pontes for the XRD measurements. The technical support of Massimo Di Menno Di Bucchianico is gratefully acknowledged.

Conflicts of Interest: The authors declare no conflict of interest.

References

1. Das, R.; Bhattacharjee, C. 16-Titanium-based nanocomposite materials for dental implant systems. In *Applications of Nanocomposite Materials in Dentistry*; Asiri, A.M., Inamuddin, M.A., Eds.; Woodhead Publishing: Sawstone, UK, 2019; pp. 271–284.
2. Zhang, Z.-Y.; Huang, T.-Y.; Zhai, D.-J.; Wang, H.-B.; Feng, K.-Q.; Xiang, L. Study on strontium doped bioactive coatings on titanium alloys surfaces by micro-arc oxidation. *Surf. Coat. Technol.* **2022**, *451*, 129045. [CrossRef]
3. Li, G.; Ma, F.; Liu, P.; Qi, S.; Li, W.; Zhang, K.; Chen, X. Review of micro-arc oxidation of titanium alloys: Mechanism, properties and applications. *J. Alloys Compd.* **2023**, *948*, 169773. [CrossRef]
4. Sasikumar, Y.; Indira, K.; Rajendran, N. Surface Modification Methods for Titanium and Its Alloys and Their Corrosion Behavior in Biological Environment: A Review. *J. Bio Tribo Corros.* **2019**, *5*, 36. [CrossRef]
5. Kuroda, P.A.B.; dos Santos, R.F.M.; Rossi, M.C.; Correa, D.R.N.; Grandini, C.R.; Afonso, C.R.M. Influence of Zr addition in β Ti-25Ta-xZr alloys on oxide formation by MAO-treatment. *Vacuum* **2023**, *217*, 112541. [CrossRef]
6. Xiao, G.; Zeng, H.; Xu, S.; Chen, C.; Zhao, Q.; Liu, X. Preparation of Ti species coating hydrotalcite by chemical vapor deposition for photodegradation of azo dye. *J. Environ. Sci.* **2017**, *60*, 14–23. [CrossRef] [PubMed]
7. Qadir, M.; Li, Y.; Wen, C. Ion-substituted calcium phosphate coatings by physical vapor deposition magnetron sputtering for biomedical applications: A review. *Acta Biomater.* **2019**, *89*, 14–32. [CrossRef]
8. Song, C.; Liu, M.; Deng, Z.-Q.; Niu, S.-P.; Deng, C.-M.; Liao, H.-L. A novel method for in-situ synthesized TiN coatings by plasma spray-physical vapor deposition. *Mater. Lett.* **2018**, *217*, 127–130. [CrossRef]
9. Azzouz, I.; Khlifi, K.; Faure, J.; Dhiflaoui, H.; Larbi, A.B.C.; Benhayoune, H. Mechanical behavior and corrosion resistance of sol-gel derived 45S5 bioactive glass coating on Ti6Al4V synthesized by electrophoretic deposition. *J. Mech. Behav. Biomed. Mater.* **2022**, *134*, 105352. [CrossRef]
10. Niu, Z.; Zhou, W.; Wang, C.; Cao, Z.; Yang, Q.; Fu, X. Fretting wear mechanism of plasma-sprayed CuNiIn coating on Ti-6Al-4V substrate under plane/plane contact. *Surf. Coat. Technol.* **2021**, *408*, 126794. [CrossRef]
11. Gao, Y.; Shen, K.; Wang, X. Microstructural evolution of low-pressure plasma-sprayed Ti–6Al–4V coatings after heat treatment. *Surf. Coat. Technol.* **2020**, *393*, 125792. [CrossRef]
12. Korkmaz, K. The effect of Micro-arc Oxidation treatment on the microstructure and properties of open cell Ti6Al4V alloy foams. *Surf. Coat. Technol.* **2015**, *272*, 72–78. [CrossRef]
13. Qi, X.; Jiang, B.; Song, R. Effects of ageing treatment on corrosion behavior of 7075 aluminum alloy coated by micro arc oxidation (MAO). *Corros. Sci.* **2022**, *199*, 110164. [CrossRef]
14. He, R.Y.; Wang, B.Y.; Xiang, J.H.; Pan, T.J. Effect of copper additive on microstructure and anti-corrosion performance of black MAO films grown on AZ91 alloy and coloration mechanism. *J. Alloys Compd.* **2021**, *889*, 161501. [CrossRef]
15. Levin, M.; Spiro, R.C.; Jain, H.; Falk, M.M. Effects of Titanium Implant Surface Topology on Bone Cell Attachment and Proliferation in vitro. *Med. Devices Evid. Res.* **2022**, *15*, 103–119. [CrossRef]
16. Mour, M.; Das, D.; Winkler, T.; Hoenig, E.; Mielke, G.; Morlock, M.M.; Schilling, A.F. Advances in Porous Biomaterials for Dental and Orthopaedic Applications. *Materials* **2010**, *3*, 2947–2974. [CrossRef]
17. Rossi, M.C.; dos Santos, R.F.; Kuroda, P.A.B.; Afonso, C.R.M. Characteristics of ceramic-like coatings obtained by plasma electrolyte oxidation on different Ti alloys. *Boletín Soc. Esp. Cerám. Vidr.* **2023**. [CrossRef]

18. Shokouhfar, M.; Dehghanian, C.; Baradaran, A. Preparation of ceramic coating on Ti substrate by Plasma electrolytic oxidation in different electrolytes and evaluation of its corrosion resistance. *Appl. Surf. Sci.* **2011**, *257*, 2617–2624. [CrossRef]
19. Ping, W.; Ting, W.; Hao, P.; Yang, G.X. Effect of $NaAlO_2$ concentrations on the properties of micro-arc oxidation coatings on pure titanium. *Mater. Lett.* **2016**, *170*, 171–174. [CrossRef]
20. Montazeri, M.; Dehghanian, C.; Shokouhfar, M.; Baradaran, A. Investigation of the voltage and time effects on the formation of hydroxyapatite-containing titania prepared by plasma electrolytic oxidation on Ti–6Al–4V alloy and its corrosion behavior. *Appl. Surf. Sci.* **2011**, *257*, 7268–7275. [CrossRef]
21. Kuroda, P.A.B.; Grandini, C.R.; Afonso, C.R.M. Anodic MAO coating formation on Ti-25Ta alloy. *Mater. Lett.* **2024**, *354*, 135377. [CrossRef]
22. Habazaki, H.; Tsunekawa, S.; Tsuji, E.; Nakayama, T. Formation and characterization of wear-resistant PEO coatings formed on β-titanium alloy at different electrolyte temperatures. *Appl. Surf. Sci.* **2012**, *259*, 711–718. [CrossRef]
23. Yao, Z.; Su, P.; Shen, Q.; Ju, P.; Wu, C.; Zhai, Y.; Jiang, Z. Preparation of thermal control coatings on Ti alloy by plasma electrolytic oxidation in K2ZrF6 solution. *Surf. Coat. Technol.* **2015**, *269*, 273–278. [CrossRef]
24. Zhang, X.; Yang, L.; Lu, X.; Lv, Y.; Jiang, D.; Yu, Y.; Peng, Z.; Dong, Z. Characterization and property of dual-functional Zn-incorporated TiO_2 micro-arc oxidation coatings: The influence of current density. *J. Alloys Compd.* **2019**, *810*, 151893. [CrossRef]
25. Duarte, L.T.; Bolfarini, C.; Biaggio, S.R.; Rocha-Filho, R.C.; Nascente, P.A.P. Growth of aluminum-free porous oxide layers on titanium and its alloys Ti-6Al-4V and Ti-6Al-7Nb by micro-arc oxidation. *Mater. Sci. Eng. C* **2014**, *41*, 343–348. [CrossRef] [PubMed]
26. Kazek-Kęsik, A.; Dercz, G.; Suchanek, K.; Kalemba-Rec, I.; Piotrowski, J.; Simka, W. Biofunctionalization of Ti–13Nb–13Zr alloy surface by plasma electrolytic oxidation. Part I. *Surf. Coat. Technol.* **2015**, *276*, 59–69. [CrossRef]
27. Khalid Naji, Q.; Mohammed Salman, J.; Mohammed Dawood, N. Investigations of structure and properties of layered bioceramic HA/TiO2 and ZrO2/Tio2 coatings on Ti-6Al-7Nb alloy by micro-arc oxidation. *Mater. Today Proc.* **2022**, *61*, 786–793. [CrossRef]
28. Wang, Y.; Jiang, B.; Lei, T.; Guo, L. Dependence of growth features of microarc oxidation coatings of titanium alloy on control modes of alternate pulse. *Mater. Lett.* **2004**, *58*, 1907–1911. [CrossRef]
29. Zhao, D.; Lu, Y.; Wang, Z.; Zeng, X.; Liu, S.; Wang, T. Antifouling properties of micro arc oxidation coatings containing Cu2O/ZnO nanoparticles on Ti6Al4V. *Int. J. Refract. Met. Hard Mater.* **2016**, *54*, 417–421. [CrossRef]
30. Gaines, S.; Luo, J.N.; Gilbert, J.; Zaborina, O.; Alverdy, J.C. Optimum Operating Room Environment for the Prevention of Surgical Site Infections. *Surg. Infect.* **2017**, *18*, 503–507. [CrossRef]
31. Shimabukuro, M.; Tsutsumi, H.; Tsutsumi, Y.; Manaka, T.; Chen, P.; Ashida, M.; Ishikawa, K.; Katayama, H.; Hanawa, T. Enhancement of antibacterial property of titanium by two-step micro arc oxidation treatment. *Dent. Mater. J.* **2021**, *40*, 592–598. [CrossRef]
32. Kozelskaya, A.I.; Verzunova, K.N.; Akimchenko, I.O.; Frueh, J.; Petrov, V.I.; Slepchenko, G.B.; Bakina, O.V.; Lerner, M.I.; Brizhan, L.K.; Davydov, D.V.; et al. Antibacterial Calcium Phosphate Coatings for Biomedical Applications Fabricated via Micro-Arc Oxidation. *Biomimetics* **2023**, *8*, 444. [CrossRef]
33. Pesode, P.A.; Barve, S.B. Recent advances on the antibacterial coating on titanium implant by micro-Arc oxidation process. *Mater. Today Proc.* **2021**, *47*, 5652–5662. [CrossRef]
34. Sedelnikova, M.B.; Komarova, E.G.; Sharkeev, Y.P.; Ugodchikova, A.V.; Mushtovatova, L.S.; Karpova, M.R.; Sheikin, V.V.; Litvinova, L.S.; Khlusov, I.A. Zn-, Cu- or Ag-incorporated micro-arc coatings on titanium alloys: Properties and behavior in synthetic biological media. *Surf. Coat. Technol.* **2019**, *369*, 52–68. [CrossRef]
35. Cardoso, G.C.; Kuroda, P.A.B.; Grandini, C.R. Influence of Nb addition on the structure, microstructure, Vickers microhardness, and Young's modulus of new β Ti-xNb-5Mo alloys system. *J. Mater. Res. Technol.* **2023**, *25*, 3061–3070. [CrossRef]
36. Cardoso, G.C.; de Almeida, G.S.; Corrêa, D.O.G.; Zambuzzi, W.F.; Buzalaf, M.A.R.; Correa, D.R.N.; Grandini, C.R. Preparation and characterization of novel as-cast Ti-Mo-Nb alloys for biomedical applications. *Sci. Rep.* **2022**, *12*, 11874. [CrossRef] [PubMed]
37. Niinomi, M.; Nakai, M. Titanium-Based Biomaterials for Preventing Stress Shielding between Implant Devices and Bone. *Int. J. Biomater.* **2011**, *2011*, 836587. [CrossRef] [PubMed]
38. Li, P.; Ma, X.; Tong, T.; Wang, Y. Microstructural and mechanical properties of β-type Ti–Mo–Nb biomedical alloys with low elastic modulus. *J. Alloys Compd.* **2020**, *815*, 152412. [CrossRef]
39. Cordeiro, J.M.; Nagay, B.E.; Ribeiro, A.L.R.; da Cruz, N.C.; Rangel, E.C.; Fais, L.M.G.; Vaz, L.G.; Barão, V.A.R. Functionalization of an experimental Ti-Nb-Zr-Ta alloy with a biomimetic coating produced by plasma electrolytic oxidation. *J. Alloys Compd.* **2019**, *770*, 1038–1048. [CrossRef]
40. Rabadia, C.D.; Liu, Y.J.; Cao, G.H.; Li, Y.H.; Zhang, C.W.; Sercombe, T.B.; Sun, H.; Zhang, L.C. High-strength β stabilized Ti-Nb-Fe-Cr alloys with large plasticity. *Mater. Sci. Eng. A* **2018**, *732*, 368–377. [CrossRef]
41. Cardoso, G.C.; Barbaro, K.; Kuroda, P.A.B.; Imperatori, L.; De Bonis, A.; Teghil, R.; Curcio, M.; Innocenzi, E.; Grigorieva, V.Y.; Vadalà, G.; et al. Incorporation of Ca, P, Mg, and Zn Elements in Ti-30Nb-5Mo Alloy by Micro-Arc Oxidation for Biomedical Implant Applications: Surface Characterization, Cellular Growth, and Microorganisms' Activity. *Coatings* **2023**, *13*, 1577. [CrossRef]
42. Cardoso, G.C.; Buzalaf, M.A.R.; Correa, D.R.N.; Grandini, C.R. Effect of Thermomechanical Treatments on Microstructure, Phase Composition, Vickers Microhardness, and Young's Modulus of Ti-xNb-5Mo Alloys for Biomedical Applications. *Metals* **2022**, *12*, 788. [CrossRef]

43. Ribeiro, A.R.; Oliveira, F.; Boldrini, L.C.; Leite, P.E.; Falagan-Lotsch, P.; Linhares, A.B.R.; Zambuzzi, W.F.; Fragneaud, B.; Campos, A.P.C.; Gouvêa, C.P.; et al. Micro-arc oxidation as a tool to develop multifunctional calcium-rich surfaces for dental implant applications. *Mater. Sci. Eng. C* **2015**, *54*, 196–206. [CrossRef] [PubMed]
44. Oliveira, F.G.; Ribeiro, A.R.; Perez, G.; Archanjo, B.S.; Gouvea, C.P.; Araújo, J.R.; Campos, A.P.C.; Kuznetsov, A.; Almeida, C.M.; Maru, M.M.; et al. Understanding growth mechanisms and tribocorrosion behaviour of porous TiO2 anodic films containing calcium, phosphorous and magnesium. *Appl. Surf. Sci.* **2015**, *341*, 1–12. [CrossRef]
45. Sousa, T.S.P.; Costa, N.d.A.d.; Correa, D.R.N.; Rocha, L.A.; Grandini, C.R. Morphology, Crystalline Structure and Chemical Composition of MAO Treated Ti-15Zr-Mo Surfaces Enriched with Bioactive Ions. *Mater. Res.* **2019**, *22*, e20190005. [CrossRef]
46. Kuroda, P.A.B.; Grandini, C.R.; Afonso, C.R.M. Surface Characterization of New β Ti-25Ta-Zr-Nb Alloys Modified by Micro-Arc Oxidation. *Materials* **2023**, *16*, 2352. [CrossRef]
47. Wang, D.-d.; Liu, X.-t.; Wang, Y.; Zhang, Q.; Li, D.-l.; Liu, X.; Su, H.; Zhang, Y.; Yu, S.-x.; Shen, D. Role of the electrolyte composition in establishing plasma discharges and coating growth process during a micro-arc oxidation. *Surf. Coat. Technol.* **2020**, *402*, 126349. [CrossRef]
48. Kuroda, P.A.B.; de Mattos, F.N.; Grandini, C.R.; Afonso, C.R.M. Influence of the heat treatment temperature on the MAO coating produced in the Ti-25Ta-25Zr alloy. *J. Mater. Res. Technol.* **2023**, *26*, 3881–3892. [CrossRef]
49. Çaha, I.; Alves, A.C.; Affonço, L.J.; Lisboa-Filho, P.N.; da Silva, J.H.D.; Rocha, L.A.; Pinto, A.M.P.; Toptan, F. Corrosion and tribocorrosion behaviour of titanium nitride thin films grown on titanium under different deposition times. *Surf. Coat. Technol.* **2019**, *374*, 878–888. [CrossRef]
50. Demirbaş, Ç.; Ayday, A. Effect of Ag concentration on structure and wear behaviour of coatings formed by micro-arc oxidation on Ti6Al4 V Alloy. *Surf. Eng.* **2021**, *37*, 24–31. [CrossRef]
51. Dos Santos, A.; Araujo, J.R.; Landi, S.M.; Kuznetsov, A.; Granjeiro, J.M.; de Sena, L.Á.; Achete, C.A. A study of the physical, chemical and biological properties of TiO_2 coatings produced by micro-arc oxidation in a Ca–P-based electrolyte. *J. Mater. Sci. Mater. Med.* **2014**, *25*, 1769–1780. [CrossRef]
52. Sikora, M.S.; Carstensen, J.; Foll, H.; Pereira, E.C. Theoretical Calculation of the Local Heating Effect on the Crystallization of TiO_2 Prepared by Sparking Anodization. *Curr. Nanosci.* **2015**, *11*, 263–270. [CrossRef]
53. Chen, K.-T.; Huang, J.-W.; Lin, W.-T.; Kuo, T.-Y.; Chien, C.-S.; Chang, C.-P.; Lin, Y.-D. Effects of Micro-Arc Oxidation Discharge Parameters on Formation and Biomedical Properties of Hydroxyapatite-Containing Flower-like Structure Coatings. *Materials* **2023**, *16*, 57. [CrossRef]
54. Navarro-Pardo, F.; Martínez-Barrera, G.; Martínez-Hernández, A.L.; Castaño, V.M.; Rivera-Armenta, J.L.; Medellín-Rodríguez, F.; Velasco-Santos, C. Effects on the Thermo-Mechanical and Crystallinity Properties of Nylon 6,6 Electrospun Fibres Reinforced with One Dimensional (1D) and Two Dimensional (2D) Carbon. *Materials* **2013**, *6*, 3494–3513. [CrossRef] [PubMed]
55. Zhang, Z.-Y.; Huang, T.-Y.; Zhai, D.-J.; Wang, H.-B.; Feng, K.-Q.; Xiang, L. Study on Zn-doped antibacterial bioactive coatings on Ti6Al4V titanium alloy surfaces by micro-arc oxidation. *Surf. Coat. Technol.* **2023**, *467*, 129724. [CrossRef]
56. Zhang, G.; Huang, S.; Li, X.; Zhao, D.; Cao, Y.; Liu, B.; Huang, Q. Oxide ceramic coatings with amorphous/nano-crystalline dual-structures prepared by micro-arc oxidation on Ti–Nb–Zr medium entropy alloy surfaces for biomedical applications. *Ceram. Int.* **2023**, *49*, 18114–18124. [CrossRef]
57. Zhang, Y.-Y.; Zhu, Y.; Lu, D.-Z.; Dong, W.; Bi, W.-J.; Feng, X.-J.; Wen, L.-M.; Sun, H.; Qi, M.-C. Evaluation of osteogenic and antibacterial properties of strontium/silver-containing porous TiO_2 coatings prepared by micro-arc oxidation. *J. Biomed. Mater. Res. Part B Appl. Biomater.* **2021**, *109*, 505–516. [CrossRef] [PubMed]
58. Bilton, M.; Brown, A.P.; Milne, S.J. Investigating the optimum conditions for the formation of calcium oxide, used for CO_2 sequestration, by thermal decomposition of calcium acetate. *J. Phys. Conf. Ser.* **2012**, *371*, 012075. [CrossRef]
59. Costa, N.A.; Correa, D.R.N.; Lisboa-Filho, P.N.; Sousa, T.S.P.; Grandini, C.R.; Rocha, L.A. Influence of the molybdenum on characteristics of oxide films produced by micro-arc oxidation on Ti-15Zr-based alloys. *Surf. Coat. Technol.* **2021**, *408*, 126856. [CrossRef]
60. Hao, Y.; Ye, Z.; Wang, L.; Ye, M.; Dong, H.; Du, Y.; Wang, C. Dual-electrolyte fabrication of micro arc oxidation coatings on Ta–12W alloy with enhanced wear resistance. *Vacuum* **2023**, *211*, 111698. [CrossRef]
61. Leśniak-Ziółkowska, K.; Kazek-Kęsik, A.; Rokosz, K.; Raaen, S.; Stolarczyk, A.; Krok-Borkowicz, M.; Pamuła, E.; Gołda-Cępa, M.; Brzychczy-Włoch, M.; Simka, W. Electrochemical modification of the Ti-15Mo alloy surface in solutions containing ZnO and $Zn_3(PO_4)_2$ particles. *Mater. Sci. Eng. C* **2020**, *115*, 111098. [CrossRef]
62. Kumari, P.; Saha, R.; Saikia, G.; Bhujel, A.; Choudhury, M.G.; Jagdale, P.; Paul, S. Synthesis of Mixed-Phase TiO_2–ZrO_2 Nanocomposite for Photocatalytic Wastewater Treatment. *Toxics* **2023**, *11*, 234. [CrossRef]
63. Nie, X.; Cai, R.; Zhao, C.; Sun, J.; Zhang, J.; Matthews, D.T.A. Advancement of plasma electrolytic oxidation towards non-valve metals. *Surf. Coat. Technol.* **2022**, *442*, 128403. [CrossRef]
64. Zhang, X.; Hang, R.; Wu, H.; Huang, X.; Ma, Y.; Lin, N.; Yao, X.; Tian, L.; Tang, B. Synthesis and antibacterial property of Ag-containing TiO_2 coatings by combining magnetron sputtering with micro-arc oxidation. *Surf. Coat. Technol.* **2013**, *235*, 748–754. [CrossRef]
65. Zhang, L.; Gao, Q.; Han, Y. Zn and Ag Co-doped Anti-microbial TiO_2 Coatings on Ti by Micro-arc Oxidation. *J. Mater. Sci. Technol.* **2016**, *32*, 919–924. [CrossRef]

66. Shimabukuro, M.; Kobayashi, M.; Kawashita, M. Metallic Substrate Influences on the Osteogenic Cell Compatibility and Antibacterial Activity of Silver-Incorporated Porous Oxide Layers Formed by Micro-Arc Oxidation. *ACS Appl. Eng. Mater.* **2023**, *1*, 2288–2294. [CrossRef]
67. Skorupska, M.; Kamedulski, P.; Lukaszewicz, J.P.; Ilnicka, A. The Improvement of Energy Storage Performance by Sucrose-Derived Carbon Foams via Incorporating Nitrogen Atoms. *Nanomaterials* **2021**, *11*, 760. [CrossRef]
68. Lara, H.H.; Romero-Urbina, D.G.; Pierce, C.; Lopez-Ribot, J.L.; Arellano-Jiménez, M.J.; Jose-Yacaman, M. Effect of silver nanoparticles on Candida albicans biofilms: An ultrastructural study. *J. Nanobiotechnol.* **2015**, *13*, 91. [CrossRef] [PubMed]
69. Chen, X.; Liao, D.; Zhang, D.; Jiang, X.; Zhao, P.; Xu, R. Friction and Wear Behavior of Graphene-Modified Titanium Alloy Micro-arc Oxidation Coatings. *Trans. Indian Inst. Met.* **2020**, *73*, 73–80. [CrossRef]
70. Li, Y.; Wang, W.; Yu, F.; Wang, D.; Guan, S.; Li, Y.; Qi, M. Characterization and cytocompatibility of hierarchical porous TiO_2 coatings incorporated with calcium and strontium by one-step micro-arc oxidation. *Mater. Sci. Eng. C* **2020**, *109*, 110610. [CrossRef]
71. Chu, Y.; Liu, P.; Chen, Y.; Li, X. Influence of Applied Voltage on Surface Morphology and Wettability of Biological Coatings on Ti6-Al-4V by Micro-Arc Oxidation Treatment. *Mater. Res.* **2020**, *23*, e20200002. [CrossRef]
72. Molaei, M.; Nouri, M.; Babaei, K.; Fattah-Alhosseini, A. Improving surface features of PEO coatings on titanium and titanium alloys with zirconia particles: A review. *Surf. Interfaces* **2021**, *22*, 100888. [CrossRef]
73. Nikoomanzari, E.; Fattah-alhosseini, A.; Pajohi Alamoti, M.R.; Keshavarz, M.K. Effect of ZrO_2 nanoparticles addition to PEO coatings on Ti–6Al–4V substrate: Microstructural analysis, corrosion behavior and antibacterial effect of coatings in Hank's physiological solution. *Ceram. Int.* **2020**, *46*, 13114–13124. [CrossRef]
74. Durdu, S.; Aktug, S.L.; Aktas, S.; Yalcin, E.; Cavusoglu, K.; Altinkok, A.; Usta, M. Characterization and in vitro properties of anti-bacterial Ag-based bioceramic coatings formed on zirconium by micro arc oxidation and thermal evaporation. *Surf. Coat. Technol.* **2017**, *331*, 107–115. [CrossRef]
75. Karabudak, F.; Yeşildal, R.; Şüküroğlu, E.E.; Şüküroğlu, S.; Zamanlou, H.; Dikbaş, N.; Bayındır, F.; Şen, S.; Totik, Y. An Investigation of Corrosion Resistance and Antibacterial Sensitivity Properties of Nano-Ag-Doped TiO_2 Coating and TiO_2 Coating Grown on NiTi Alloy with the Micro-Arc Oxidation Process. *Arab. J. Sci. Eng.* **2017**, *42*, 2329–2339. [CrossRef]
76. Lv, Y.; Wu, Y.; Lu, X.; Yu, Y.; Fu, S.; Yang, L.; Dong, Z.; Zhang, X. Microstructure, bio-corrosion and biological property of Ag-incorporated TiO2 coatings: Influence of Ag_2O contents. *Ceram. Int.* **2019**, *45*, 22357–22367. [CrossRef]
77. Durdu, S.; Aktug, S.L.; Korkmaz, K.; Yalcin, E.; Aktas, S. Fabrication, characterization and in vitro properties of silver-incorporated TiO_2 coatings on titanium by thermal evaporation and micro-arc oxidation. *Surf. Coat. Technol.* **2018**, *352*, 600–608. [CrossRef]
78. *ISO 10993-5*; Biological Evaluation of Medical Devices. Part 5: Tests for In Vitro Cytotoxicity. ISO: Geneva, Switzerland, 2009.
79. Chen, H.; Cheng, D.-H.; Huang, S.-C.; Lin, Y.-M. Comparison of flexural properties and cytotoxicity of interim materials printed from mono-LCD and DLP 3D printers. *J. Prosthet. Dent.* **2021**, *126*, 703–708. [CrossRef] [PubMed]
80. Jablonská, E.; Kubásek, J.; Vojtěch, D.; Ruml, T.; Lipov, J. Test conditions can significantly affect the results of in vitro cytotoxicity testing of degradable metallic biomaterials. *Sci. Rep.* **2021**, *11*, 6628. [CrossRef]
81. Srivastava, G.K.; Alonso-Alonso, M.L.; Fernandez-Bueno, I.; Garcia-Gutierrez, M.T.; Rull, F.; Medina, J.; Coco, R.M.; Pastor, J.C. Comparison between direct contact and extract exposure methods for PFO cytotoxicity evaluation. *Sci. Rep.* **2018**, *8*, 1425. [CrossRef]
82. Shimabukuro, M.; Tsutsumi, Y.; Yamada, R.; Ashida, M.; Chen, P.; Doi, H.; Nozaki, K.; Nagai, A.; Hanawa, T. Investigation of Realizing Both Antibacterial Property and Osteogenic Cell Compatibility on Titanium Surface by Simple Electrochemical Treatment. *ACS Biomater. Sci. Eng.* **2019**, *5*, 5623–5630. [CrossRef]